Journal of Fluids and Structures 129 (2024) 104154

Contents lists available at ScienceDirect

Journal of Fluids and Structures

journal homepage: www.elsevier.com/locate/jfs

Reconstructing flexible body vortex-induced vibrations using machine-vision and predicting the motions using semi-empirical models informed with transfer learned hydrodynamic coefficients

Andreas P. Mentzelopoulos [a,1,*], Emile Prele [b,1], Dixia Fan [c], Jose del Aguila Ferrandis [a], Themistoklis Sapsis [a], Michael S. Triantafyllou [a]

[a] Department of Mechanical Engineering, Massachusetts Institute of Technology, Cambridge, MA 02139, USA
[b] Department of Mechatronics, École normale supérieure, Rennes, 35000, France
[c] School of Engineering, Westlake University, Hangzhou, Zhejiang 310024, China

ARTICLE INFO

Keywords:
Flexible body vortex induced vibrations (VIV)
Added mass coefficient
Lift coefficient
Machine learning
Machine vision
Optimization
Transfer learning
Experimental data

ABSTRACT

This work assesses the validity of transfer learning the hydrodynamic coefficient database, consisting of the added mass and lift coefficients, applicable to flexible bodies undergoing vortex-induced vibrations. Specifically, the hydrodynamic coefficient database learned on data collected by Braaten and Lie (2005) are used to predict the motions observed during in house bare riser model experiments at the MIT Towing Tank. A fully immersed vertical flexible riser model with a length-to-diameter ratio of 145 is towed at different flow speeds and top tensions. Motion is tracked using underwater cameras and the motions are reconstructed using a machine-vision framework eliminating the need for expensive sensing hardware. The vibration amplitude, frequency, and mode shape are determined and the results are compared with those in the literature. Finally, blind predictions of the in-house observed experiments are made using the software VIVA informed with transfer learned hydrodynamic coefficients learned on the experiments by Braaten and Lie (2005).

1. Introduction

Observations of vortex induced vibrations (VIV) date back to antiquity, when the Aeolian tones, sounds created by pressure fluctuations induced by winds passing over taut strings were recognized. The first sketches of vortices date back to Leonardo da Vinci in the early 16th century. Today, VIV have become a problem of interest to both theoreticians, due to the complex underlying mechanisms involved, and engineers, due to the practical significance of mitigating the fatigue damage VIV can cause to offshore structures and equipment such as marine risers and offshore wind turbines.

The underlying driving mechanism of VIV is vortex formation; specifically, the periodic shedding of vortices formed in the wake behind bluff bodies placed within cross-currents (Triantafyllou et al., 2016). The vortex shedding frequency in rigid bodies is known as the Strouhal frequency. For flexibly mounted or flexible bodies, the vortex formation frequency can be entrained away from the Strouhal frequency and coincides with the frequency of vibration in a phenomenon known as lock-in Navrose and Mittal (2016). This occurs across a wide range of oscillating frequencies resembling a nonlinear resonance (Park et al., 2016). VIV have amplitudes of vibrations that do not typically exceed one to two body diameters (Bernitsas et al., 2019). Rigid cylinder VIV are the canonical

* Corresponding author.
E-mail address: ament@mit.edu (A.P. Mentzelopoulos).
[1] Equal contribution.

https://doi.org/10.1016/j.jfluidstructs.2024.104154
Received 1 December 2023; Received in revised form 3 April 2024; Accepted 8 June 2024

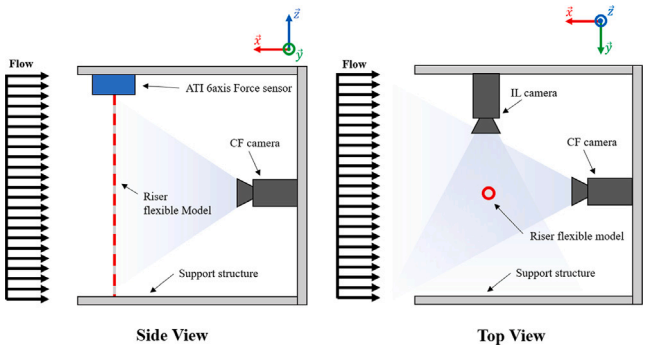

Fig. 1. Schematic of the experimental setup. The riser model was vertically positioned at the center of a supporting frame, which was affixed to the carriage of the towing tank. Two cameras were affixed to the supporting frame facing perpendicular directions, to capture the cross-flow and in-line vibrations respectively.

problem for study of the phenomenon (Williamson and Roshko, 1988; Zdravkovich, 1996; Wu et al., 2014). Flexible body VIV are qualitatively similar to flexibly mounted rigid body vibrations, but with the added complexity that they are not span-wise uniform as the flexible body undergoes spatially traveling and/or standing waves (Wang et al., 2021; Triantafyllou et al., 2016; Fan et al., 2019).

Riser motion reconstruction has been done by leveraging the physics-based modal decomposition technique (Mukundan, 2008; Wang et al., 2019; Triantafyllou et al., 1999; Kharazmi et al., 2021; Mentzelopoulos et al., 2023) developed to model vibrations of continuous flexible bodies, such as beams (Rao, 1995). Predictions of VIV motions given the vibrating body's geometry, material properties, and inflow velocity profile are possible using computational fluids dynamics (CFD) simulations (Wu et al., 2014; Wang et al., 2021) or using semi-empirical prediction codes such as VIVA (Zheng et al., 2011), VIVANA (Larsen et al., 2017, 2001; Wu et al., 2020), and Shear7 (Vandiver, 1999; Resvanis and Vandiver, 2022). They all model the vibrating body as a flexible beam vibrating under the excitation of a hydrodynamic force; the force is modeled based on experimentally derived coefficients. The accuracy of such codes relies on the quality of the hydrodynamic coefficients used in modeling the hydrodynamic force (Rudy et al., 2022; Mentzelopoulos, 2022). In this work, we transfer-learn the hydrodynamic coefficients of a flexible body undergoing VIV: using the hydrodynamic coefficients learned on a uniform 38 m riser model (Braaten and Lie, 2005) in uniform flow to predict the motions of a 0.87 m riser model towed in house at the MIT Towing Tank in a uniform flow.

The paper is organized as follows: first, the conducted experiments are detailed and the resulting motions are presented and compared to literature. A thorough presentation of the experimental data analysis done by leveraging machine vision methods is presented. Second, semi-empirical code VIVA is used to predict the motions of the experiments conducted in house using the hydrodynamic coefficients learned on the experiments by Braaten and Lie (2005), also known in the literature as the Norwegian Deep Water Programme (NDP) experiments.

2. Methods

In this section, we detail the experimental facilities, setup, and procedures followed in order to study the flexible cylinder's vortex-induced vibrations and asses whether transfer learned hydrodynamic coefficients used with semi-empirical prediction program VIVA can predict the motions observed experimentally.

2.1. Experimental setup

Experiments were conducted at the MIT Towing Tank, a facility consisting of a 35 m × 2.5 m × 1.2 m testing tank equipped with a carriage capable of reaching speeds exceeding 2 m/s as well as a flow visualization window.

Fig. 1 illustrates the experimental setup schematically. A solid aluminum frame was used to support the flexible cylinder; the riser model was placed vertically at the center of the structure. An ATI 6 degree of freedom force sensor was attached to the top end of the riser to measure its tension. Two GoPro Hero 11 cameras were attached to the supporting frame facing perpendicular directions to capture videos of the riser's motion in the cross-flow and in-line directions, respectively.

The riser model was constructed out of urethane rubber infused with tungsten powder. Specifically, Smooth-On PMC-724 urethane rubber was mixed with powdered tungsten to increase the model's density and to achieve a mass-ratio of $m^* = \frac{\rho}{\rho_{H_2O}} = 3$. The mixture was poured into a right cylindrical mold with a fishing line (mono-filament nylon, "Berkley Trilene Big Game 25LB rated") placed along its centerline to provide tension. The diameter of the fishing line was 0.48 mm. The model's length was 870 mm with a 6 mm diameter. The aspect ratio of the model riser was $L/D = 145$. The natural frequencies were calculated to be 1.71 Hz at 1N of axial tension and 4.18 Hz at 6N of axial tension. Equidistant markers were spray-painted red on the riser model resembling a zebra-patterning to enable motion tracking using cameras. Three underwater light fixtures were used to enhance visibility underwater. The model's ends were clamped on the supporting frame and the model was separated from the frame by a distance much greater than the body's diameter O(> 10D) (see Fig. 2).

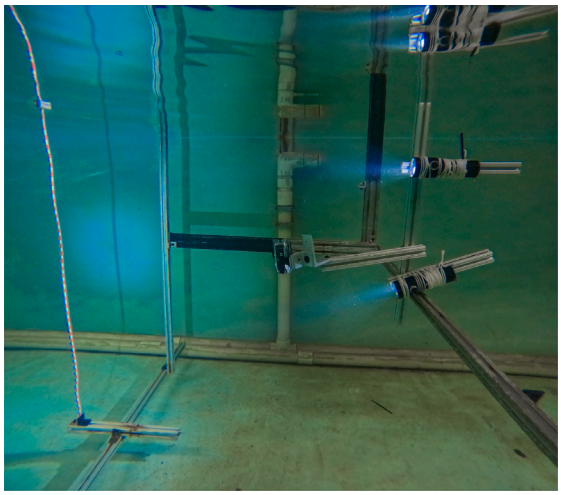

Fig. 2. Experimental setup. The riser model is supported by a solid aluminum frame. The frame is attached to the towing tank carriage. Two cameras are used to record the motions in the cross-flow and in-line directions, respectively. The riser is marked red at various locations along its span.

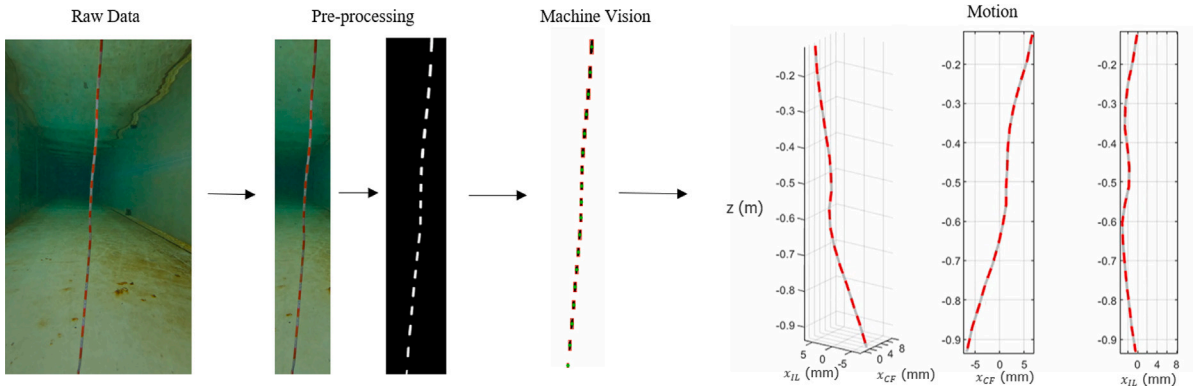

Fig. 3. Processing pipeline of raw data from the experiments. From left to right: raw video frame, cropped frame, frame with zebra patterning masked, machine-vision tracking, and 3D virtual reconstruction of the observed motion. Initial video footage pre-processing involved HSV color space masking. The masked images were then fed into a machine-vision tracking algorithm leveraging Kalman filters for motion tracking, determining the marker positions across the video frames. (For interpretation of the references to color in this figure legend, the reader is referred to the web version of this article.)

The flexible cylinder was towed at five different speeds, namely 0.2, to 0.7 m/s, at increments of 0.1 m/s. The towing results in a uniform incoming flow profile along the x direction, as shown in Fig. 1. Recordings of the motions were captured at a resolution of 1080p (1920 $\times$ 1080 pixels). The sampling rate was 120 fps. The Reynolds number across the experiments ranged between $1000 \lesssim Re \lesssim 3500$.

3. Results and discussion

3.1. Motion reconstruction via machine vision

The goal of the experiments was to reconstruct the model riser's motion in both the cross-flow and the in-line directions. Raw data for this study were the video recordings captured by the two underwater cameras, eliminating the need for multiple expensive strain or acceleration sensors. To proceed with the motion reconstructions, an efficient image processing pipeline was developed, driven by powerful multi-object tracking algorithms leveraging Kalman filters. The processing pipeline was made up of three main tasks as detailed below and visualized in Fig. 3:

- Pre-processing: Creating a black and white mask of the zebra patterned red markers on the riser.
- Multi-object tracking using Kalman filters: tracking the position (in pixels) of the zebra-stripped red markers on the body across the full video recording.
- Post-processing: Scaling the tracked positions from pixels to physical (length) units.

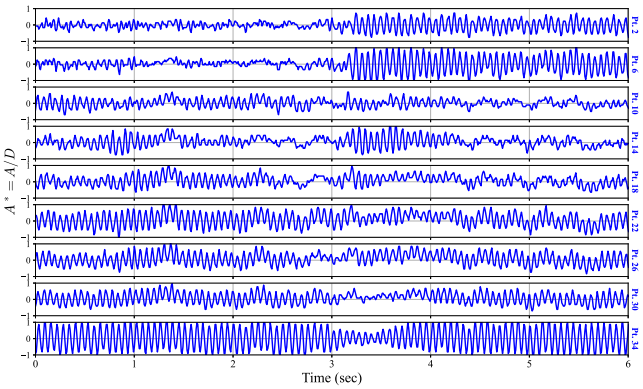

Fig. 4. Cross-flow displacement normalized by the body's diameter, $A^* = A/D$, at 9 equidistant locations of the riser along the span. The towing speed was set at $U = 0.6$ m/s, and the top tension applied was $T = 4.64$ N. The resulting true reduced velocity was $U^* = \frac{U}{f_{osc} * D} \approx 6.0$. The variability in response amplitude across both the span and time highlights the non-uniform and unsteady nature of the response.

For pre-processing, the black and white mask was created by leveraging the HSV (hue, saturation, value) representation of the images. Specifically, red colors, which may be easily identified using the hue values of the pixels were separated from the image and were masked as white, while all other pixels were set to black. One may easily identify the red markers on the raw frame in Fig. 3 which are then masked white during pre-processing while the rest of the image is set to black. It should be emphasized that the HSV representation allows one to correctly identify the markers regardless of how bright (well lit) they are in the unprocessed frame.

The masked images were then fed to a vision algorithm which detected each colored marker as a blob and recorded its position as that of the pixel closest to its centroid. As such, multiple blobs were tracked in each image and Kalman filtering was leveraged to ensure that tracking of each blob was consistent across multiple frames and no mixing in the trajectories occurred across the full video recordings.

Having tracked the position of the markers on the body in pixels (rather than physical units), scaling was achieved by multiplying the trajectories with an appropriate factor λ which was determined by leveraging a known reference length. In this case, a measure was recorded parallel to the riser (i.e. in a vertical orientation). The scaling factor was calculated according to the following equation.

$$\lambda = \frac{L_{ref}}{N_{pixels}} \tag{1}$$

where N_{pixels} are the number of pixels used (1920 pixels for 1080p resolution in the vertical direction) and L_{ref} is the reference length captured from the bottom to the top of the frame. The cross-flow and in-line data were finally synced in order to reconstruct the full three dimensional motion of the riser's VIV. Synchronization of the motion was performed by giving a light signal once both cameras were recording. Uncertainty introduced by the motion tracking was estimated to about 2 pixels.

Fig. 4 illustrates the recorded vibrations in the cross-flow direction at 9 different equidistant locations along the riser model's span normalized by the model's diameter. Six seconds are shown in the figure. The tow speed (i.e. incoming uniform flow velocity) was $U = 0.6$ m/s and the top tension was $T = 4.64$ N. As is illustrated in Fig. 4, the recorded vibration amplitude varied significantly along the body's span and was dynamic exhibiting fluctuations in time. However, the riser's vibrations did not exceed approximately one body diameter as expected at the recorded Reynolds numbers. The response amplitude variance along both space (i.e. body span) and time indicate the non-uniformity of the response as well as its dynamic behavior.

A total of 29 experimental runs were conducted. The resulting motions were determined and various responses were recorded including various structural modes and responses consisting of standing waves, traveling waves, and the superposition of the two. Fig. 5 illustrates the root mean square VIV recorded from each experiment. The cross-flow vibrations are shown as blue while the in-line vibrations are shown as red. The span of the riser, normalized by length, is plotted on the x-axis, while the amplitude, normalized by the diameter is plotted on the y-axis. Flow speed increases from left to right (from 0.2 m/s to 0.7 m/s) while tension increases from top to bottom.

Greater amplitude vibrations were recorded in the cross-flow direction compared to the in-line direction; a higher order structural mode was recorded in the in line vibrations for the same flow speed and tension. As expected, for the same flow speed the mode number associated with the response decreased as tension increased. Additionally, the vibration mode increased with flow speed for a given static top tension. It should be noted that the tension increased when the model was towed and the vibrations initiated.

In some cases, the results exhibit significant asymmetries in the cross-flow vibrations due to traveling wave responses. Examples of such behaviors are the experiment with $T = 1.3$ N and $U = 0.2$ m/s (row 1, column 1 in Fig. 5) and $T = 5.19$ N and $U = 0.7$ m/s (row 4, column 4 in Fig. 5). In the first example (row 1, column 1) the recorded vibration amplitude towards the top of the riser model ($L^* \approx 1$) was significantly greater than that recorded close to the bottom end ($L^* \approx 0$). A traveling wave response was dominant with waves traveling towards the top end of the riser. The "opposite" is observed in the second example (row 4, column

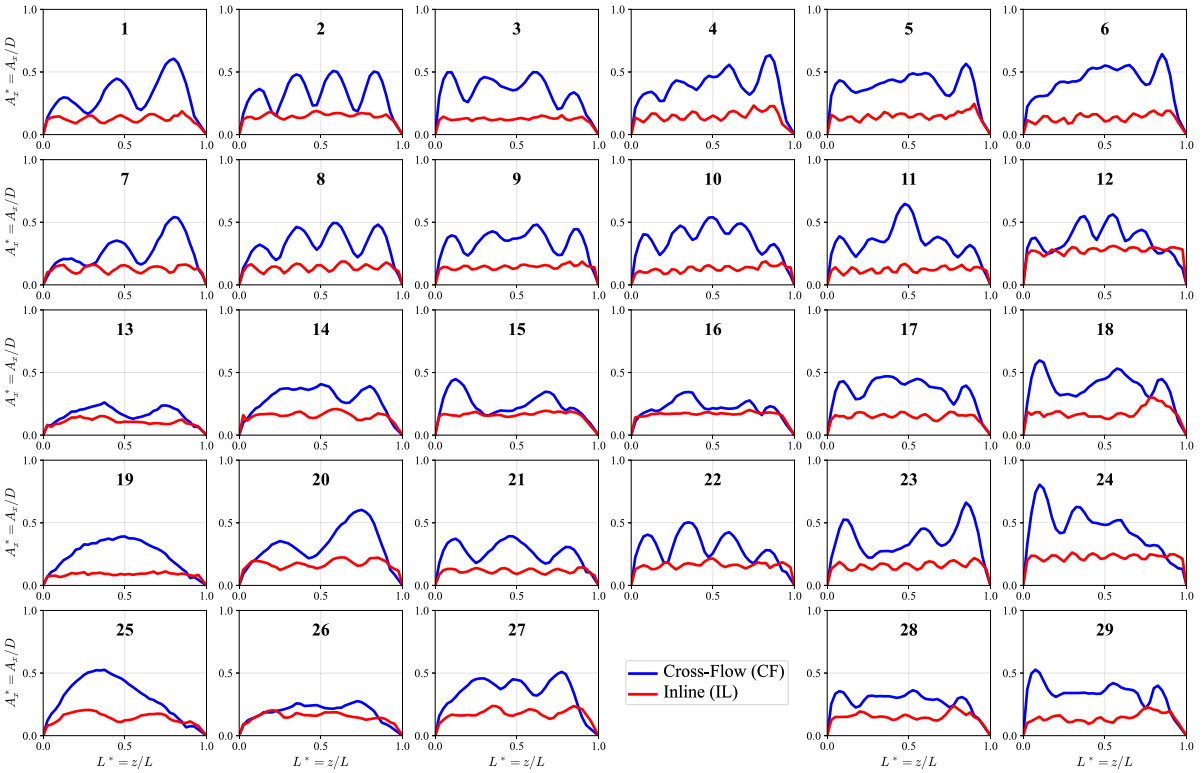

Fig. 5. Root-mean-square motions of the recorded vibrations. The y-axis depicts the amplitude normalized by the diameter, denoted as $A^* = A/D$, while the x-axis represents the body position normalized by length, indicated as $L^* = z/L$. Cross-flow vibrations are shown in blue, and in-line vibrations are shown in red. The plot progresses from left to right, corresponding to an increase in flow speed (ranging from 0.2 m/s to 0.7 m/s), and from top to bottom, corresponding to an increase in tension. Various structural modes are evident in the plot. (For interpretation of the references to color in this figure legend, the reader is referred to the web version of this article.)

4), the vibrations towards the bottom end were greater and the amplitude decreased towards the top end of the riser. A traveling wave response was recorded with waves propagating towards the bottom end of the structure.

More symmetric cross-flow responses, indicating a standing wave response were also recorded; for example in the experiment with $T = 4.92\ N$ and $U = 0.2$ m/s (row 3, column 1 in Fig. 5), a standing wave at the second mode is observed.

3.2. Comparison with literature

In this section, we compare our results to those obtained by others in the literature. Given that most studies focus on cross-flow vibrations only, since they are most often responsible for fatigue damage on vibrating risers, in-line data will not be used in this section.

In the literature the frequency of vibration of flexible beams is non-dimensionalized and sometimes referred to as the "Strouhal number", a misnomer, since the Strouhal number refers to rigid, non-vibrating bodies, where the Strouhal number is constant and is only a function of the Reynolds number. In contrast, as already mentioned, in vibrating bodies the frequency of vibration can be entrained away from the Strouhal frequency in a phenomenon called wake capture. Also, the effect of the added mass, which varies with the frequency (primarily) and amplitude of vibration, is to alter the natural frequency of a vibrating cylinder; this is especially pronounced for low reduced mass; as a result, the frequency of vibration is not equal to the Strouhal frequency nor to the natural frequency in quiescent fluid. In addition, in-line motion has a strong effect on the frequency of vortex formation, moving further away from the Strouhal frequency. We define, then, a nondimensional *reduced frequency* f_o^*, which is the non-dimensionalized recorded frequency of vibration.

$$f_o^* = \frac{f_v\ D}{U} \tag{2}$$

where f_v is the vortex shedding frequency (equal to the body vibrating frequency in VIV since synchronization occurs, aka "lock-in"). f_o^* has a strong dependence on the Reynolds number Re, as shown in Fig. 6, and can be quite different from the Strouhal number of $St \approx 0.20$.

Fig. 6 illustrates f_o^* as a function of Reynolds obtained by five different studies as marked in the figure. For cases 3, 4, and 5 data are from Lienhard (1966). Studies 1 and 2 study the VIV of flexible cylinders vibrating underwater, while studies 3, 4, and

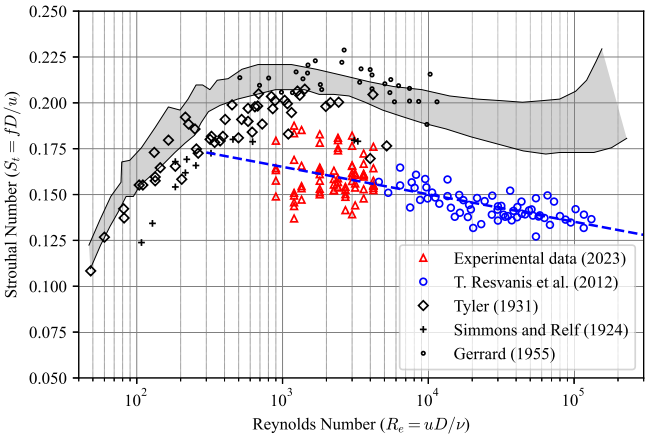

Fig. 6. Non-dimensional *reduced* frequency of vibration f_o^* as a function of Reynolds number obtained in five different studies, including this work. The studies are the following: 1. this study (red triangles), 2. Resvanis et al. (2012) (blue circles), 3. Tyler, 1931 (gray diamonds), 4. Simmons and Reif, 1924 (gray plus signs), and 5. Gerrard, 1955 (gray circles).

5, were conducted using flexibly mounted rigid cylinders allowed to vibrate in the cross-flow direction only in wind tunnels. Two main conclusions can be made from this plot: (a) Rigid (flexibly mounted) bodies vibrating in cross-flow only and flexible bodies do not vibrate at the same f_o^* as function of Re; specifically, rigid cylinder VIV exhibit a higher f_o^* in the range $1000 < Re < 10,000$ compared to flexible bodies, (b) This study agrees qualitatively and extends the finding of Resvanis et al. (2012) that a logarithmic trend may be identified on average for flexible cylinders' f_o^* as a function of Re in the range $1000 < Re < 100,000$. The relationship is $f_o^* = -0.0065 \log Re + 0.21$. We note that the data obtained in this study exhibit a higher variance from the mean compared to those obtained by Resvanis et al. (2012) as is evident in the figure. This is due to the wake entrainment, and the effects of added mass and in-line motion on the frequency of vibration.

3.3. Identified responses in the cross-flow direction

In this section, we present the structural responses observed during the experiments. It should be noted that a wide variety of responses was observed including both traveling and standing waves. In addition, the motions observed were dynamic and evolved rapidly throughout the experiments with various responses and transitions being recorded within each experiment.

Fig. 7 illustrates a selection of experiments in which the 1st, 2nd, 3rd, 4th, and 5th modes were recorded (cross-flow). Each plot in the top row of the figure illustrates the rms of the vibration recorded and may be used to identify the observed mode number. The amplitude of the vibration is plotted on the y-axis against body span which is plotted on the x-axis. The second row includes surface plots of the recorded vibration at different time intervals in which steady-state responses were observed. The y-axis measures time, the x-axis measures body span and the vibration displacement is highlighted on the plane. For example, on the very bottom left subplot (row 2, col 1), approximately 1.2 s of the recorded vibration are illustrated; a standing wave response of the 1st mode is evident. In the second (row 2, col 2), third (row 2, col 3), and fourth (row 2, col 4) plots, standing waves of the second, third, and fourth modes are recorded, respectively. The fifth (row 2, col 5) plots are still dominated by standing waves, although some crests do appear to travel indicating the superposition of traveling and standing waves; in both cases the crests are migrating from the top end of the body towards the bottom end.

It should be noted that these steady-state responses that were recorded represent a small fraction of the observed motions. Fig. 8 illustrates the observed motion of a riser vibrating for a total of 8 s. Body span is plotted on the y-axis against time on the x-axis; the vibration displacement is highlighted on the plane. The riser shown was towed at 0.4 m/s with a top tension of 2.92 N. The figure illustrates how the riser's motion evolved as a function of time; a summary of the observations is given below.

- From 0 s to 3 s: 4th mode traveling waves propagating from the top end ($L^* = 1$) to the bottom end ($L^* = 0$) of the riser (~50 cycles).
- From 3 s to 4 s: transition region where a superposition of 4th mode standing and traveling waves is observed (~10 cycles).
- From 4 s to 5.5 s: 4th mode standing waves (~5 cycles).
- From 5.5 s to 6.5 s : 4th mode traveling waves propagating from body's top end ($L^* = 1$) towards the bottom ($L^* = 0$) end (~10 cycles).
- From 7 s to 7.25 s: 4th mode standing waves (~5 cycles).
- From 7.25 s to 8 s: 4th mode traveling waves propagating from body's bottom end ($L^* = 0$) towards the body's top end ($L^* = 1$) (~10 cycles).

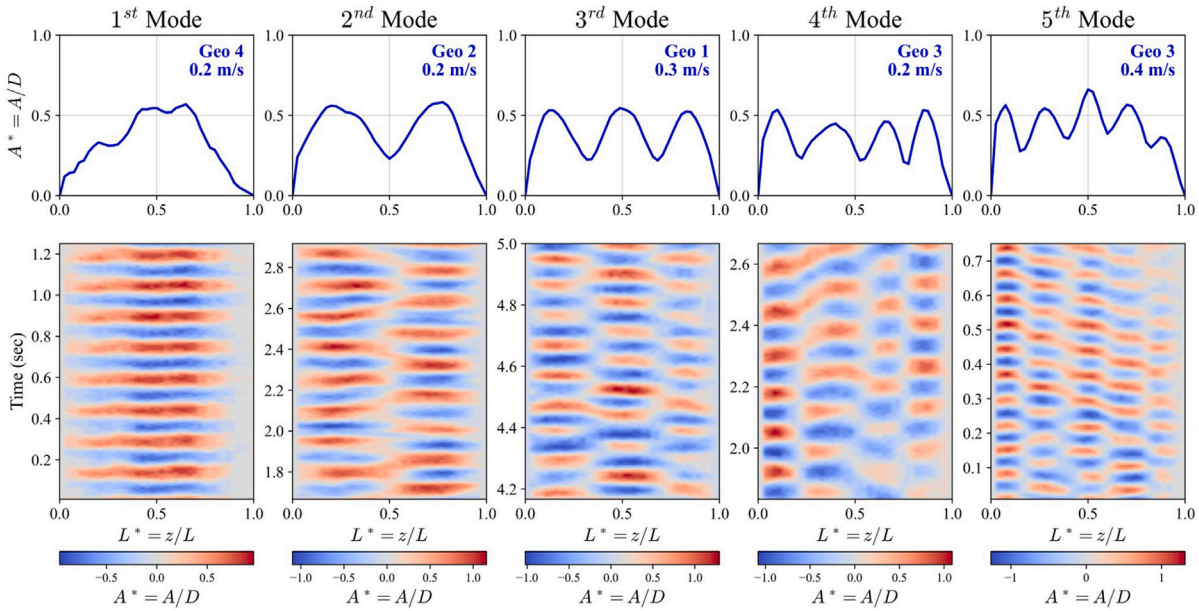

Fig. 7. A selection of time intervals during which vibrations of the 1st, 2nd, 3rd, 4th, and 5th modes were recorded. In the top row of the figure, each plot illustrates the root mean square (rms) of the recorded vibration, serving as a means to identify the observed mode number. The y-axis represents the amplitude of the vibration, while the x-axis depicts the body span; motion is highlighted on the plane. In the second row, surface plots showcase the recorded vibration at selected intervals where steady-state responses were observed.

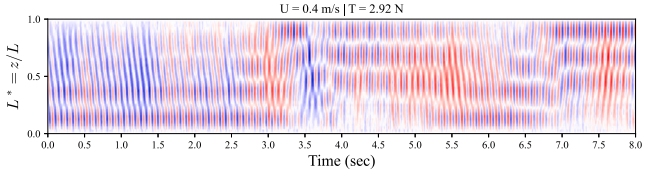

Fig. 8. Observed motion of a riser vibrating (cross-flow) for a total of 8 s. The y-axis measures body span, while the x-axis shows time. Vibration displacement is highlighted on the plane. The riser model was towed at a speed of 0.4 m/s, with a top tension of 2.92 N. The true reduced velocity was $U^* \approx 5.5$. The figure provides insight into the evolution of the riser's motion in time, showcasing regions characterized by traveling waves and standing waves, along with transitional areas.

The richness and variety of responses and transitions that are evident in Fig. 8 are typical of the motions recorded throughout the experiments. The plethora of motions highlights the complexity of the underlying mechanisms involved, which can result in various different responses for the same flow condition and tension. It should be noted that although the geometric and towing configuration is symmetric (uniform body in uniform flow), asymmetries in both the mode shapes and the amplitudes are evident, caused by the breaking of symmetry in the hydrodynamic loads: this is expected since the vortex shedding is not perfectly symmetric or steady.

3.4. Transfer learning the added-mass and lift coefficients

Although predicting the exact VIV motion as a function of time for a flexible body is challenging, semi-empirical models (Triantafyllou et al., 1999; Vandiver, 1999; Larsen et al., 2001) have been successful in predicting the motion observed on average: specifically these models can give reasonably accurate estimates of the rms of the vibration of flexible bodies given their geometry, material properties, and incoming flow profile. Such models are used by industry for riser design and simulation. However, their predictive power relies on the added mass and lift coefficients (also referred to as the hydrodynamic coefficient database) used to estimate the force applied on the body by the flow. Estimating those coefficients is nontrivial and requires either performing rigid body vibration experiments (Gopalkrishnan, 1993; Resvanis and Vandiver, 2022) or machine-learning the coefficients using data (Rudy et al., 2022; Mentzelopoulos et al., 2022).

In this section we assess the validity of transfer learning hydrodynamic coefficients across different experimental datasets. In doing so, we also validate how useful (in terms of predictive power) flow-structure interaction information is encoded in the learned coefficients, which may be inferred from one dataset and then used to predict a different one.

3.4.1. Modeling flexible body VIV

We model the flexible body as a continuous flexible beam with variable tension, mass properties, and geometric properties vibrating under the excitation of a hydrodynamic force (Triantafyllou et al., 1999; Zheng et al., 2011; Vandiver, 1999). The equation governing the motion is as follows (Rao, 1995).

$$m\frac{\partial^2 y}{\partial t^2} + b\frac{\partial y}{\partial t} - \frac{\partial}{\partial z}(T\frac{\partial y}{\partial z}) + \frac{\partial^2}{\partial z^2}(EI\frac{\partial^2 y}{\partial z^2}) = f \tag{3}$$

where m denotes the mass per unit length, b corresponds to damping, T is tension, EI is the flexural rigidity, and f is the excitation force (the hydrodynamic force). We note that T and EI may assume different values as functions of span. The dimensions of Eq. (3) are force per unit length.

In VIV, we expect sinusoidal vibration modes as follows:

$$y(z,t) = \mathrm{Re}\left[Y(z)e^{i\omega t}\right] \tag{4}$$

where $Y(x)$ is the complex valued amplitude of vibration along the span and ω is the frequency of vibration. We denote by Re the real part; not to be confused with Re, the Reynolds number. The hydrodynamic force is assumed to have the following form (Triantafyllou et al., 1999), corresponding to a component in anti-phase with acceleration (the added mass force) and a component in phase with velocity as shown below.

$$f = \mathrm{Re}\left[\left(\frac{1}{4}C_m\pi\rho D^2\omega^2 Y + \frac{i}{2}C_{lv}\rho U^2 D\frac{Y}{|Y|}\right)e^{i\omega t}\right] \tag{5}$$

where ρ is the fluid-density, D is the body's diameter, and U is the incoming flow velocity. The hydrodynamic coefficients C_m and C_{lv} are used to estimate the hydrodynamic force and are assumed known a priori.

Eqs. (3), (4), and (5) yield an eigenvalue problem which may be solved to determine the frequency and mode shape of the riser vibration under the excitation of the hydrodynamic force.

$$\frac{d^2}{dz^2}(EI\frac{d^2Y}{dz^2}) - \frac{d}{dz}(T\frac{dY}{dz}) + \left[-(m+\alpha C_m)\omega^2 + ib\omega\right]Y = iC_{lv}qD\frac{Y}{|Y|} \tag{6}$$

where $\alpha = \frac{1}{4}\rho\pi D^2$ and $q = \frac{1}{2}\rho U^2$. Eq. (6) is a well defined nonlinear eigenvalue problem given appropriate boundary conditions; the nonlinearity originates from the dependence of the hydrodynamic coefficients C_m and C_{lv} on the amplitude $Y(z)$ and the vibration frequency ω.

3.4.2. Learning the added mass and lift coefficients

The dependence of the hydrodynamic coefficients on the frequency ω and amplitude Y of the vibration is mainly influenced by the following nondimensional quantities (Triantafyllou et al., 1999; Vandiver, 1999; Fan, 2019): true reduced frequency f_r, nondimensional amplitude A^*, and Reynolds number Re.

$$f_r = \frac{\omega D}{2\pi U} \qquad A^* = \frac{A}{D} \qquad Re = \frac{U\,D}{\nu} \tag{7}$$

where ν is the fluid's kinematic viscosity. For a given speed of tow, the coefficients depend only on the true reduced frequency, while the lift coefficient depends on both the true reduced frequency and the nondimensional amplitude as shown below (Rudy et al., 2022).

$$C_m = f(f_r) \qquad C_{lv} = f(f_r, A^*) \tag{8}$$

Given a known mapping between the hydrodynamic coefficients and the nondimensional quantities, one may solve the eigenvalue problem (Eq. (6)) and estimate a riser's motions.

3.4.3. Parametrizing the hydrodynamic coefficients

The geometry of the most comprehensive database for hydrodynamic coefficients, as documented by Gopalkrishnan (1993), served as the foundation for the coefficient parametrization.

Since C_{lv} depends on both f_r and A^*, three intermediate curves were introduced to fully characterize the geometry of the surface. This parametrization is illustrated in Fig. 9. Contours parallel to the A^* axis, where $C_{lv} = f(A^*)$ with f_r constant (depicted in blue in Fig. 9), were represented by two piecewise linear segments. Additionally, the contour $C_{lv} = f(f_r)$ at $A^* = 0$ (depicted in red in Fig. 9) and $A^*_c = f(f_r)$ (depicted in purple in Fig. 9) were utilized, both represented by piecewise linear double peak curves. Corner point coordinates were employed to define parameters, and the shapes were smoothed using a softplus function.

In a similar fashion, the added mass coefficient, C_m which is a function of f_r only was parametrized as piece-wise linear. The parametrization is shown in Fig. 10.

A total of nineteen parameters ($\boldsymbol{p} : p_i,\ i \in [1,19]$) were chosen to define the four curves constituting a comprehensive hydrodynamic coefficient database: 1. C_m vs. f_r, 2. $C_{lv,0}$ vs. f_r, 3. A^c vs. f_r, and 4. Clv vs. A. The final parameter (p_{19}) acted as the scaling factor for the softplus function.

The mathematical formulation of the reduced-order model is detailed as follows. First, the softplus function is defined:

$$sf(x,\boldsymbol{p}) = p_{19}\cdot\ln(1+\exp\frac{x}{p_{19}}) \tag{9}$$

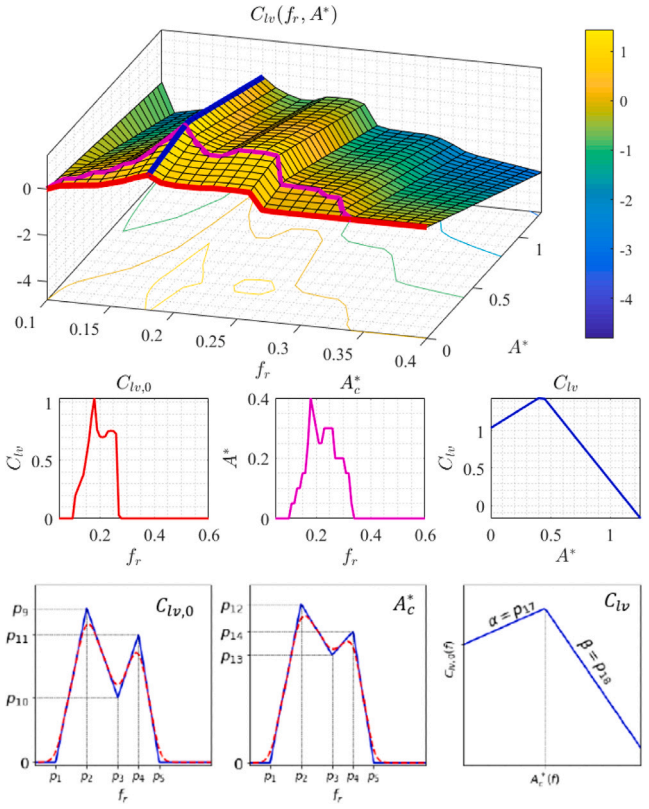

Fig. 9. (Top) Surface plot of Gopalkrishnan (1993) $C_{lv} = f(f_r, A^*)$. The projection of the surface on the $f_r - A^*$ plane is plotted. The contours used as references for the parametrization are highlighted on the surface plot. (Middle) The contours used as references for the parametrization are plotted individually. (Bottom) Shapes defined by the parametrization are illustrated.

Here, p_{19} serves as a scaling constant. Subsequently, the C_m curve is parametrized by Eq. (10):

$$\begin{aligned}\hat{C}_m(f_r, \boldsymbol{p}) = p_{15} &+ \frac{p_{16} - p_{15}}{p_6 - p_2}[sf(f_r - p_2) - sf(f_r - p_6)] \\ &+ \frac{1 - p_{16}}{p_8 - p_7}[sf(f_r - p_7) - sf(f_r - p_8)]\end{aligned} \tag{10}$$

where $\hat{C}_m(f_r, \boldsymbol{p})$ represents the parametric form of the C_m curve. Similarly, $Clv, 0$ can be represented as in Eq. (11):

$$\begin{aligned}\hat{C}_{lv,0}(f_r, \boldsymbol{p}) = &\frac{p_9}{p_2 - p_1}[sf(f_r - p_1) - sf(f_r - p_2)] \\ &+ \frac{p_{10} - p_9}{p_3 - p_2}[sf(f_r - p_2) - sf(f_r - p_3)] \\ &+ \frac{p_{11} - p_{10}}{p_4 - p_3}[sf(f_r - p_3) - sf(f_r - p_4)] \\ &+ \frac{-p_{11}}{p_5 - p_4}[sf(f_r - p_4) - sf(f_r - p_5)]\end{aligned} \tag{11}$$

where $\hat{C}_{lv,0}(f_r, \boldsymbol{p})$ denotes the parametric form of the $Clv, 0$ curve. Likewise, the A_c^* curve is expressed parametrically as shown in Eq. (12):

$$\begin{aligned}\hat{A}_c^*(f_r, \boldsymbol{p}) = &\frac{p_{12}}{p_2 - p_1}[sf(f_r - p_1) - sf(f_r - p_2)] \\ &+ \frac{p_{13} - p_{12}}{p_3 - p_2}[sf(f_r - p_2) - sf(f_r - p_3)] \\ &+ \frac{p_{14} - p_{13}}{p_4 - p_3}[sf(f_r - p_3) - sf(f_r - p_4)] \\ &+ \frac{-p_{13}}{p_5 - p_4}[sf(f_r - p_4) - sf(f_r - p_5)]\end{aligned} \tag{12}$$

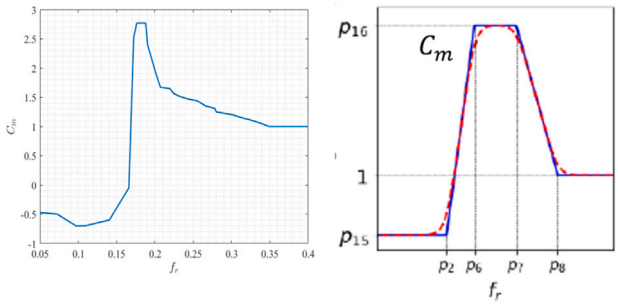

Fig. 10. (Left) (Gopalkrishnan, 1993) $C_m = f(f_r)$. (Right) parametrization.

Table 1
Riser specifications.

Specification	Value
Material	Urethane rubber, tungsten powder
Length (L)	870 mm
Drag (outer) diameter	6 mm
Aspect ratio (L/D)	145
mass ratio (m^*)	3
weight (N)	0.48 N
mass-per-unit-length (μ)	0.11 kg/m
density	3000 kg/m^3

Table 2
Parameter constraints.

p_1	$p_2 - p_8$	p_9	$p_{10} - p_{14}$	p_{15}	p_{16}	p_{17}	p_{18}	p_{19}
(0.0, 0.5)	(0, 1)	(0, 2)	(0, 1)	(−1, 1)	(1, 5)	(0.1, 5)	(0.1, 5)	(0, 0.005)

where $\hat{A}_c^*(f_r, \boldsymbol{p})$ represents the parametric form of the non-dimensional critical amplitude A^c. Finally, the lift coefficient, Clv, is determined according to Eq. (13):

$$C_{lv}(A^*, \boldsymbol{p}) = \begin{cases} C_{lv,0} + p_{17} \cdot A^* & if\, A^* \le A_c^* \\ C_{lv,0} + p_{17} \cdot A_c^* - p_{18} \cdot (A^* - A_c^*) & if\, A^* > A_c^* \end{cases} \tag{13}$$

The parameters' values were constrained based on empirical knowledge as depicted in Table 2. Notably, the parametric model permits shared parameters among the 4 curves defining the complete parametric database. For instance, parameters $p_1 - p_5$ are shared between the $C_{lv,0} = f(f_r)$ and the $A_c^* = f(f_r)$ curves. The complete parametrization can be visualized in Figs. 9 and 10.

3.4.4. Learning the hydrodynamic coefficients

Given the hydrodynamic coefficients, one can solve the EVP of Eq. (6) and estimate VIV motions. However, the reverse problem may be formulated in which given the flexible body's motion, one can use it to learn the mapping between the coefficients and the nondimensional quantities. This can be achieved as follows.

- parametrize the mappings of Eq. (8) using a set of parameters $\boldsymbol{p}$ as $C_m = f(\boldsymbol{p})$ and $C_{lv} = f(\boldsymbol{p})$.
- Initialize the parameters. This can be done at random (Rudy et al., 2022) or by projecting an estimate of a known database on the parametric space (Mentzelopoulos et al., 2022, 2023).
- Use the database $\boldsymbol{p}$ to make predictions of the known motions by solving the eigenvalue problem of Eq. (6).
- Update the parameters according to the discrepancy between motion prediction using $\boldsymbol{p}$ and observations from data.

The following cost function, which is a weighted sum of the mean square error of the vibration and the frequency, may be used to evaluate the fitness of the learned parameters and minimized to learn the hydrodynamic coefficients.

$$J(\boldsymbol{p}) = \frac{1}{L}\int_0^L (Y - \hat{Y}(\boldsymbol{p}))^2 dz + \lambda(f - \hat{f}(\boldsymbol{p}))^2 \tag{14}$$

where the balancing factor λ may be chosen arbitrarily. Thus, the learned mapping will be

$$C_m = f(\boldsymbol{p}^*) \qquad C_{lv} = f(\boldsymbol{p}^*) \qquad \boldsymbol{p}^* = \arg\min_{\boldsymbol{p}} J(\boldsymbol{p}) \tag{15}$$

A stochastic coordinate descent method (Rudy et al., 2021) may be used to optimize the cost function.

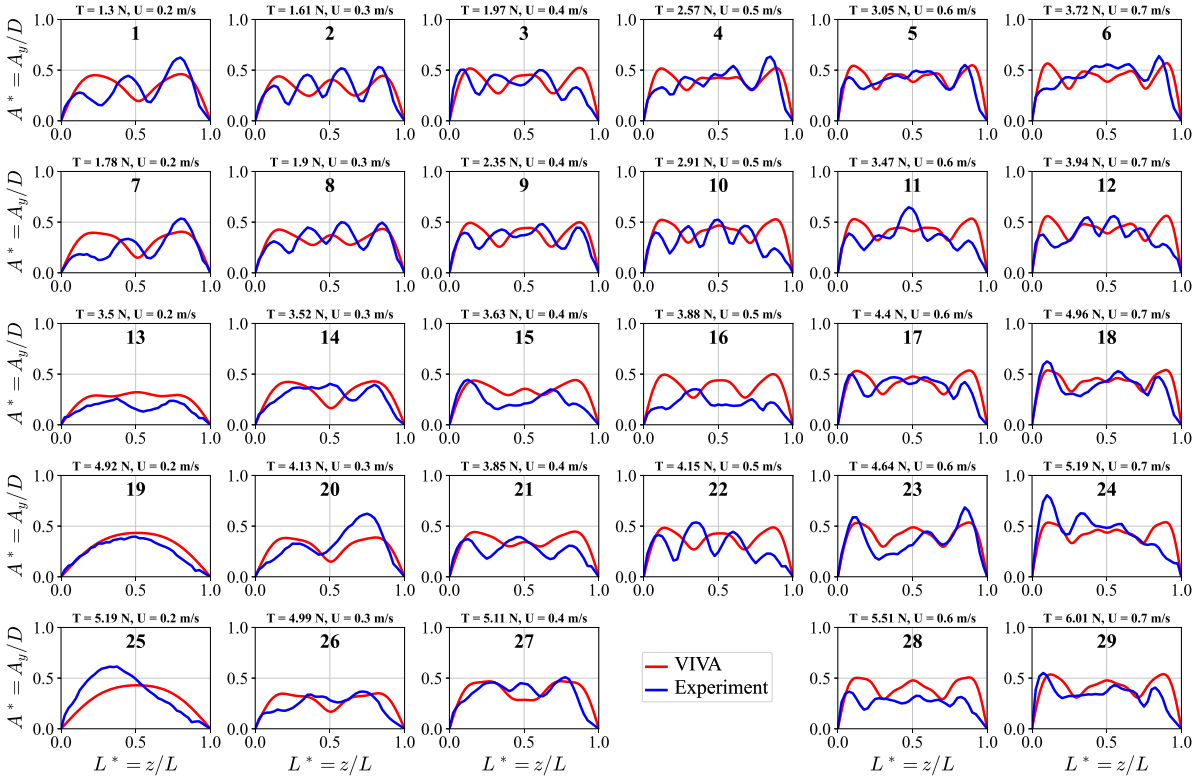

Fig. 11. Cross flow root-mean-square motions of in-house experiments and blind predictions of software VIVA using transfer learned hydrodynamic coefficients on data from Braaten and Lie (2005). Predictions of cross-flow motion using model VIVA are colored red, while observed cross-flow motion from in-house experiments is shown as blue. The nondimensional amplitude A^* is plotted on the y-axis against body span on the x-axis. We underscore that the predictions made by model VIVA are blind, meaning that only information related to the model's geometry, material properties, and flow conditions were input into the software. Despite being agnostic to the specific input data, the predictions offer reasonably accurate estimates of the observed motion. This result validates that meaningful and interpretable information regarding the flow-structure interaction is encoded in the hydrodynamic database representations used by the model, as has been suggested in the literature. (For interpretation of the references to color in this figure legend, the reader is referred to the web version of this article.)

Table 3
Braaten and Lie (2005) riser model specifications.

Specification	Value
Material	Fiberglass
Length	38 m
Drag diameter	30 mm
Aspect ratio	1407
Mass ratio	1.62

3.4.5. Predictions using transfer learned hydrodynamic coefficients

The reverse problem was solved for the data collected by Braaten and Lie (2005) as part of the Norwegian Deep Water Programme, on a 38 m long fiberglass riser model towed in a uniform flow. The tow velocities were 0.3 m/s up to 2.4 m/s, in 0.1 m/s increments. The particulars of the riser used are shown in Table 3.

By comparing the riser model used in this study (Table 1) and the riser model used by Braaten and Lie (2005) (Table 3), it is evident that the two models were made out of different materials, had a different aspect ratio, different mass ratio, length, and diameter. In addition, the Reynolds numbers were different. Specifically, in the experiments conducted for this study the Reynolds numbers were approximately in the range $10^3 < Re < 10^4$ while in Braaten and Lie (2005) the Reynolds numbers were approximately in the range $10^4 < Re < 10^5$.

Fig. 11 illustrates the predictive capabilities of model VIVA (Zheng et al., 2011) informed with the hydrodynamic coefficients obtained by optimizing Eq. (14) on the data collected by Braaten and Lie (2005). Specifically, each subplot includes two curves: 1. cross-flow motion predictions of model VIVA (red) 2. cross-flow motion observation from experiments conducted in this study (blue). The nondimensional amplitude A^* is plotted on the y-axis against body span plotted on the x-axis. We note that model VIVA's predictions are blind in the sense that no information other than the model's geometry and flow conditions were fed to the software.

Notably, the predictions provide reasonably accurate estimates of the observations: the amplitude and mode shape are predicted to reasonable accuracy.

Although the predictions could certainly be improved by further training the model on the data obtained during experiments (Rudy et al., 2022; Mentzelopoulos et al., 2022, 2023), by using the hydrodynamic coefficients obtained by Braaten and Lie (2005) as an initial condition for the optimization routine and training on the specific data collected during the experiments, this result validates that important information of the flow-structure interaction is indeed encoded in the hydrodynamic databases as has been claimed in literature (Resvanis and Vandiver, 2022; Zheng et al., 2011; Gopalkrishnan, 1993).

We expect similarities in the vibration of our uniform riser model and that measured by Braaten and Lie (2005) due to the similar geometry and flow profile (uniform straight risers in uniform flow) and we observe that information learned on one experimental dataset is relevant to the other. We do anticipate however that since the Reynolds numbers and other factors such as the aspect ratio and material properties were different, not all relevant information from one experiment could be learned using the other. As such, we do not expect high accuracy predictions without further refinement of the hydrodynamic databases. The reasonably accurate estimates of the model with transfer learned coefficients suggest however that the (interpretable) learned representations (hydrodynamic coefficients) after training on experiments are meaningful and can certainly be used as a good starting point for further transfer learning. The result also suggests that a database learned on more data of various geometries and flow profiles could perhaps be universal, in the sense that a single database could be able to make successful predictions of different kinds of risers under a plethora of flow conditions.

4. Conclusions

In this work, the VIV motions of a straight uniform riser model towed in a uniform flow were reconstructed using machine vision eliminating the need for multiple expensive sensors. An algorithm leveraging Kalman filters for motion tracking was developed and will be open-sourced by the authors on the Open VIV Repository hosted by MIT. The obtained motions illustrate the richness of the structural responses observed in flexible body VIV, such as traveling waves, standing waves, and superpositions of the two. The observed responses were dynamic and unsteady indicating the complex outcomes of riser VIV even for seemingly unchanged experimental conditions highlighting the complexity of underlying mechanisms involved. The results obtained fit well in literature and agree with the results obtained by Resvanis et al. (2012), while extending to lower Reynolds numbers.

The added mass and lift coefficients of the experiments conducted by Braaten and Lie (2005) were learned by optimizing the discrepancy between motion predictions using model VIVA (Zheng et al., 2012; Triantafyllou et al., 1999) and experimental observations. The learned coefficients were then used to predict the motions observed during in-house experiments conducted on a riser model of similar geometry but different aspect ratio, mass ratio, material properties, and Reynolds number. Reasonable agreement is observed between the predictions and observations suggesting that the hydrodynamic coefficients provide meaningful (interpretable) representations of the flow-structure interactions as has been suggested in literature (Resvanis and Vandiver, 2022; Gopalkrishnan, 1993; Larsen et al., 2001; Zheng et al., 2011; Vandiver, 1999). The hydrodynamic coefficients may not only be used to understand the flow-structure interaction physics and to make predictions, but can also be used as initial conditions for further transfer learning.

CRediT authorship contribution statement

Andreas P. Mentzelopoulos: Writing – review & editing, Writing – original draft, Visualization, Validation, Software, Methodology, Investigation, Formal analysis, Conceptualization. **Emile Prele:** Writing – review & editing, Writing – original draft, Visualization, Software, Methodology, Investigation, Formal analysis, Conceptualization. **Dixia Fan:** Writing – review & editing, Writing – original draft, Visualization, Supervision, Software, Project administration, Methodology, Investigation, Formal analysis, Conceptualization. **Jose del Aguila Ferrandis:** Writing – review & editing, Writing – original draft, Visualization, Software, Methodology, Investigation, Formal analysis, Data curation, Conceptualization. **Themistoklis Sapsis:** Writing – review & editing, Supervision, Resources, Project administration, Methodology, Conceptualization. **Michael S. Triantafyllou:** Writing – review & editing, Supervision, Software, Resources, Project administration, Methodology, Funding acquisition, Conceptualization.

Declaration of competing interest

The authors declare that they have no known competing financial interests or personal relationships that could have appeared to influence the work reported in this paper.

Data availability

Data will be made available on request.

Acknowledgments

The authors would like to acknowledge support from the DigiMaR Consortium, MathWorks, and the Onassis Foundation.

References

Bernitsas, M.M., Ofuegbe, J., Chen, J.-U., Sun, H., 2019. Eigen-solution for flow induced oscillations (VIV and galloping) revealed at the fluid-structure interface. In: ASME 2019 38th International Conference on Ocean, Offshore and Arctic Engineering. American Society of Mechanical Engineers Digital Collection.

Braaten, H., Lie, H., 2005. NDP Riser High Mode VIV Tests Main Report. MARINTEK report, Trondheim, Norway.

Fan, D., 2019. Mapping the hydrodynamic properties of flexible and rigid bodies undergoing vortex-induced vibrations (Ph.D. thesis). Massachusetts Institute of Technology.

Fan, D., Wang, Z., Triantafyllou, M.S., Karniadakis, G.E., 2019. Mapping the properties of the vortex-induced vibrations of flexible cylinders in uniform oncoming flow. J. Fluid Mech. 881, 815–858.

Gopalkrishnan, R., 1993. Vortex-induced forces on oscillating bluff cylinders (Ph.D. thesis). Massachusetts Institute of Technology.

Kharazmi, E., Wang, Z., Fan, D., Rudy, S., Sapsis, T., Triantafyllou, M.S., Karniadakis, G.E., 2021. From data to assessment models, demonstrated through a digital twin of marine risers. In: Offshore Technology Conference. OnePetro.

Larsen, C., Lie, H., Passano, E., Yttervik, R., Wu, J., Baarholm, G., 2017. VIVANA—Theory Manual, Version 4.10. 1. SINTEF Ocean. Trondheim, Norway.

Larsen, C.M., Vikestad, K., Yttervik, R., Passano, E., Baarholm, G.S., 2001. VIVANA Theory Manual. Marintek, Trondheim, Norway.

Lienhard, J.H., 1966. Synopsis of Lift, Drag, and Vortex Frequency Data for Rigid Circular Cylinders. Vol. 300, Washington State University, Technical Extension Service.

Mentzelopoulos, A.P., 2022. Learning hydrodynamic coefficient databases for vortex induced vibration prediction of marine risers using sparse sensor measurements Master's thesis. Massachusetts Institute of Technology.

Mentzelopoulos, A.P., del Águila Ferrandis, J., Rudy, S., Sapsis, T., Triantafyllou, M.S., Fan, D., 2022. Data-driven prediction and study of vortex induced vibrations by leveraging hydrodynamic coefficient databases learned from sparse sensors. Ocean Eng. 266, 112833. http://dx.doi.org/10.1016/j.oceaneng.2022.112833.

Mentzelopoulos, A.P., Fan, D., Resvanis, T., Sapsis, T., Triantafyllou, M.S., 2023. Physics-based unsupervised learning of vortex-induced vibrations from riser field experimental stain data. In: The 33rd International Ocean and Polar Engineering Conference. OnePetro.

Mukundan, H., 2008. Vortex-induced vibration of marine risers: motion and force reconstruction from field and experimental data. Massachusetts Institute of Technology.

Navrose, Mittal, S., 2016. Lock-in in vortex-induced vibration. J. Fluid Mech. 794, 565–594. http://dx.doi.org/10.1017/jfm.2016.157.

Park, H., Kumar, R.A., Bernitsas, M.M., 2016. Suppression of vortex-induced vibrations of rigid circular cylinder on springs by localized surface roughness at $3\times 104 \leq Re \leq 1.2\times 105$. Ocean Eng. 111, 218–233.

Rao, S.S., 1995. Mechanical vibrations. Addison Wesley, Boston, MA.

Resvanis, T.L., Jhingran, V., Vandiver, J.K., Liapis, S., 2012. Reynolds number effects on the vortex-induced vibration of flexible marine risers. In: International Conference on Offshore Mechanics and Arctic Engineering. Vol. 44922, American Society of Mechanical Engineers, pp. 751–760.

Resvanis, T.L., Vandiver, J.K., 2022. Efficient measurement of hydrodynamic coefficients for vibrating cylinders at supercritical Reynolds numbers. J. Fluids Struct. 108, 103427.

Rudy, S., Fan, D., del Aguila Ferrandis, J., Sapsis, T.P., Triantafyllou, M.S., 2022. Optimized parametric hydrodynamic databases provide accurate response predictions and describe the physics of vortex-induced vibrations. J. Fluids Struct. 112, 103607.

Rudy, S., Fan, D., Ferrandis, J.d.A., Sapsis, T., Triantafyllou, M.S., 2021. Learning optimal parametric hydrodynamic database for vortex-induced crossflow vibration prediction. arXiv preprint arXiv:2104.05887.

Triantafyllou, M.S., Bourguet, R., Dahl, J., Modarres-Sadeghi, Y., 2016. Vortex-induced vibrations. In: Springer Handbook of Ocean Engineering. Springer, pp. 819–850.

Triantafyllou, M.S., Triantafyllou, G.S., Tein, Y.S., Ambrose, B.D., 1999. Pragmatic riser VIV analysis. In: Offshore Tech. Conf. Offshore Technology Conference.

Vandiver, J., 1999. SHEAR7 Program User Manual. Massachusetts Institute of Technology, Cambridge, MA.

Wang, Z., Fan, D., Triantafyllou, M.S., 2021. Illuminating the complex role of the added mass during vortex induced vibration. Phys. Fluids 33 (8), 085120.

Wang, J., Fu, S., Baarholm, R., Zhang, M., Liu, C., 2019. Global motion reconstruction of a steel catenary riser under vessel motion. Ships Offshore Struct. 14 (5), 442–456.

Williamson, C., Roshko, A., 1988. Vortex formation in the wake of an oscillating cylinder. J. Fluids Struct. 2 (4), 355–381. http://dx.doi.org/10.1016/S0889-9746(88)90058-8.

Wu, W., Bernitsas, M.M., Maki, K., 2014. RANS simulation versus experiments of flow induced motion of circular cylinder with passive turbulence control at $35{,}000 \leq R_e \leq 130{,}000$. J. Offshore Mech. Arct. Eng. 136 (4).

Wu, J., Jin, J., Yin, D., Lie, H., Passano, E., Sævik, S., Tognarelli, M.A., Grytøyr, G., Andersen, T., Karunakaran, D., et al., 2020. Time domain VIV analysis tool VIVANA-TD: validations and improvements. In: International Conference on Offshore Mechanics and Arctic Engineering. Vol. 84409, American Society of Mechanical Engineers, V008T08A031.

Zdravkovich, M., 1996. Different modes of vortex shedding: An overview. J. Fluids Struct. 10 (5), 427–437.

Zheng, H., Modarres-Sadeghi, Y., Dahl, J., Triantafyllou, M.S., 2012. Inline-crossflow coupled vortex induced vibrations of long flexible cylinders. In: International Conference on Offshore Mechanics and Arctic Engineering. Vol. 44922, American Society of Mechanical Engineers, pp. 743–749.

Zheng, H., Price, R., Modarres-Sadeghi, Y., Triantafyllou, G.S., Triantafyllou, M.S., 2011. Vortex-induced vibration analysis (VIVA) based on hydrodynamic databases. In: International Conference on Offshore Mechanics and Arctic Engineering. Vol. 44397, pp. 657–663.